

Structure-Preserving Transfer of Grad–Shafranov Equilibria to Magnetohydrodynamic Solvers

Rushan Zhang^a, Golo Wimmer^{b,1}, Qi Tang^{a,2,*}

^a*School of Computational Science and Engineering, Georgia Institute of Technology, Atlanta, GA 30332.*

^b*Theoretical Division, Los Alamos National Laboratory, Los Alamos, NM 87545.*

Abstract

Magnetohydrodynamic (MHD) solvers used to study dynamic plasmas for magnetic confinement fusion typically rely on initial conditions that describe force balance, which are provided by an equilibrium solver based on the Grad–Shafranov (GS) equation. Transferring such equilibria from the GS discretization to the MHD discretization often introduces errors that lead to unwanted perturbations to the equilibria on the level of the MHD discretization. In this work, we identify and analyze sources of such errors in the context of finite element methods, with a focus on the force balance and divergence-free properties of the loaded equilibria. In particular, we reveal three main sources of errors: (1) the improper choice of finite element spaces in the MHD scheme relative to the poloidal flux and toroidal field function spaces in the GS scheme, (2) the misalignment of the meshes from two solvers, and (3) possibly under-resolved strong gradients near the separatrix. With this in mind, we study the impact of different choices of finite element spaces, including those based on compatible finite elements. In addition, we also investigate the impact of mesh misalignment and propose to conduct mesh refinement to resolve the strong gradients near the separatrix. Numerical experiments are conducted to demonstrate equilibria errors arising in the transferred initial conditions. Results show that force balance is best preserved when structure-preserving finite element spaces are used and when the MHD and GS meshes are both aligned and refined. Given that the poloidal flux is often computed in continuous Galerkin spaces, we further demonstrate that projecting the magnetic field into divergence-conforming spaces is optimal for preserving force balance, while projection into curl-conforming spaces, although less optimal for force balance, weakly preserves the divergence-free property.

Keywords: Compatible Finite Element, Grad–Shafranov Equation, Magnetohydrodynamics, Magnetic Confinement Fusion

1. Introduction

The magnetohydrodynamic (MHD) equations are widely used for simulating long-time instabilities such as disruptions in magnetic confinement fusion (MCF) devices [1, 2, 3]. Such instabilities may arise from small perturbations to an MHD equilibrium [4], and thereby, clean and accurate equilibrium solutions as initial conditions are essential for stability analysis. In axisymmetric devices, equilibrium solutions are typically obtained by solving the Grad–Shafranov (GS) equation, which expresses the magnetic field in axisymmetric (r, z) -coordinates in terms of its poloidal and toroidal components, using the poloidal magnetic flux function Ψ and the toroidal magnetic field profile $f(\Psi)$ [1]. Although axisymmetry allows the field to be represented using 2D scalar functions, time-dependent MHD simulations of inherently 3D instabilities still require a full 3D vector field as the initial condition. In particular, in order to express the Lorentz force term, a discrete

*Corresponding authors

Email addresses: rzhangbq@gatech.edu (Rushan Zhang), gwimmer@lanl.gov (Golo Wimmer), qtang@gatech.edu (Qi Tang)

¹Research was partially supported by the Laboratory Directed Research and Development program of Los Alamos National Laboratory (LANL), under project number 20240261ER, as well as the U.S. Department of Energy Office of Fusion Energy Sciences Base Theory Program, at LANL under contract No. 89233218CNA000001.

²Research was partially supported by the U.S. Department of Energy Advanced Scientific Computing Research program of Mathematical Multifaceted Integrated Capability Center (MMICC).

representation of the initial magnetic field \mathbf{B} and the corresponding current density vector \mathbf{J} is required. Consequently, converting GS solver outputs for Ψ and f into the full magnetic vector field is necessary.

There are various strategies for solving the GS equation and loading GS-solver-based solutions into transient MHD solvers. The standard approach is to store Ψ -data on a Cartesian grid along with a list of 1D arrays for different profiles that are needed to reconstruct full fields. This often follows formats used by the widely used EFIT code [5], in which Ψ is stored in a 2D array and the toroidal field function f and pressure p are documented as arrays depending on normalized Ψ . The magnetic field may then be reconstructed on the Cartesian grid using, e.g., finite differences, and can then be interpolated onto the MHD solver grid [6, 7, 8]. This workflow motivated the recent advance of several finite-difference-based GS solvers that use Cartesian grids [9, 10], cut-cells [11] and structured adaptive grids [12].

While GS solvers are commonly based on finite differences, large-scale MHD solvers for axisymmetric MCF devices are often based on finite elements [2, 3]. When providing equilibria for these MHD solvers, the GS solver should naturally be based on finite elements [13, 14, 15]. However, a systematic study on how to transfer solutions between the two finite element solvers is currently missing, and, in practice, ad hoc approaches are often applied to address this gap. For instance, [16] adopts a spectral element basis and uses a spectral element expansion to compute the field values required by the MHD solver, while the Jorek code [3] re-solves the GS equation on the same mesh as the MHD solver and incorporates Ψ directly into the transient MHD evolution after loading from a free-boundary GS solver. In fact, re-solving has been found to be necessary to achieve a good force balance in the MHD simulation [17].

In practice, the choice of discretization in GS solvers and the strategy of transferring to a given MHD grid significantly affects the quality of the initial state for stability analysis. For instance, [7] reports a force imbalance in the initial condition and requires additional damping of the force residuals before the MHD evolution. Such errors in the equilibrium solution, as transferred onto the MHD grid, potentially originate from three sources: (1) incompatibilities between the GS and MHD discretizations, (2) interpolation between unaligned computational meshes, and (3) sharp gradients near the separatrix.

In this work, we analyze the above error sources, with particular focus on the first source, which arises from the choice of GS vs MHD discretizations. Our starting point is an MFEM-based free-boundary GS solver [15]. Based on the GS equilibria attained from this solver, we consider zero-pressure equilibria, and focus on the Lorentz force term, as it is relatively complex compared to the pressure gradient term. Our investigation is carried out within a compatible finite element framework. The compatible finite element method is a mixed finite element method that introduces a sequence of finite element spaces designed to form differential complexes, in which one finite element space is mapped to another by differential operators [18, 19]. Compatible finite elements have been considered extensively for Faraday’s law and more generally MHD as a constrained transport method [20, 21, 22, 23], ensuring an exact zero-divergence property for the magnetic field (in a weak or a strong sense). Within this framework, given the differential operation occurring in the definition of \mathbf{B} as a function of Ψ , we identify sets of compatible finite element spaces such that the GS-to-MHD transfer error is minimized. Based on this identification, together with meshing related considerations, the main contributions of this work are as follows:

- We propose that the numerical GS-to-MHD transfer error is minimized when (1) the finite element spaces used for the magnetic field \mathbf{B} are the spaces that are contained in the same compatible finite element chain as the initial finite element spaces where Ψ and f reside, (2) the mesh in the toroidal cross-section of the transient MHD solver is aligned with the 2D mesh of the GS solver and (3) the mesh is sufficiently refined along the separatrix.
- We describe a projection path and a mesh refinement strategy that reflects the above considerations for minimizing the transfer error. In particular, one of our novel projection paths also naturally preserves the magnetic field’s divergence-free property. This eliminates the need for an initial divergence cleaning step within the MHD solver. A divergence cleaning step may otherwise lead to additional perturbations to the MHD equilibrium.
- We implement the proposed projection path in MFEM [24], demonstrating the importance of both meshing *and* function space considerations necessary to preserve the approximate MHD equilibrium in the MHD solver’s initial conditions.

The remainder of this paper is structured as follows. In Section 2, we derive our quantities of interest related to transferring data from the GS solver to the MHD solver. In Section 3, we review the compatible finite element method and discuss it in the context of MHD equilibria. In Section 4, we introduce our new loading procedure based on compatible finite elements, including a discussion on the magnetic field's divergence-free property and the resulting discrete MHD equilibrium Lorentz force terms. In Sections 5 and 6, we describe our code implementation and present numerical results, respectively. Finally, in Section 7, we end with a conclusion of our work.

2. Governing equations

2.1. Grad-Shafranov equation

In MHD, given a tokamak domain Ω , the non-dimensionalized plasma velocity momentum equation can be written as

$$\rho \left(\frac{\partial \mathbf{u}}{\partial t} + \mathbf{u} \cdot \nabla \mathbf{u} \right) + \beta \nabla p + \mathbf{B} \times \mathbf{J} = \mathbf{0}, \quad (1)$$

for density ρ , flow velocity \mathbf{u} , pressure p , magnetic field \mathbf{B} , non-dimensional internal-to-magnetic energy ratio $\beta \ll 1$, and current density

$$\mathbf{J} = \nabla \times \mathbf{B}. \quad (2)$$

Typically, in tokamaks, the plasma is considered to be in an axisymmetric equilibrium state where the pressure gradient and Lorentz force are in balance, given by

$$\beta \nabla p + \mathbf{B} \times \mathbf{J} = \mathbf{0}. \quad (3)$$

To construct a pressure field p and magnetic field \mathbf{B} that satisfy (3), we switch to cylindrical coordinates (r, ϕ, z) and drop any dependence on the ϕ -coordinate in p and \mathbf{B} . Next, we express the magnetic field through the magnetic vector potential $\mathbf{A} = (A_r, A_\phi, A_z)$, such that $\mathbf{B} = \nabla_c \times \mathbf{A}$, for cylindrical coordinate curl

$$\nabla_c \times \mathbf{A} = \left(\frac{1}{r} \frac{\partial A_z}{\partial \phi} - \frac{\partial A_\phi}{\partial z} \right) \mathbf{e}_r + \left(\frac{\partial A_r}{\partial z} - \frac{\partial A_z}{\partial r} \right) \mathbf{e}_\phi + \frac{1}{r} \left(\frac{\partial(r A_\phi)}{\partial r} - \frac{\partial A_r}{\partial \phi} \right) \mathbf{e}_z, \quad (4)$$

where $\mathbf{e}_r, \mathbf{e}_\phi, \mathbf{e}_z$ denote the unit vectors in cylindrical coordinates. Using axisymmetry and the definition of the curl in axisymmetric coordinates, we then have

$$\mathbf{B} = \nabla_c \times (A_\phi \mathbf{e}_\phi) + \left(\frac{\partial A_r}{\partial z} - \frac{\partial A_z}{\partial r} \right) \mathbf{e}_\phi. \quad (5)$$

Next, we transfer our axisymmetric equations to the 2D (r, z) -plane for which we use the natural embedding of axisymmetric 3D fields in (r, ϕ, z) -space to 2D fields in (r, z) -space

$$\sim_\phi: A(r, \phi, z) \rightarrow A(r, z), \quad (6)$$

and define

$$A_\phi \sim_\phi \frac{1}{r} \Psi(r, z), \quad \frac{\partial A_r}{\partial z} - \frac{\partial A_z}{\partial r} \sim_\phi \frac{1}{r} f(r, z), \quad (7)$$

for fields Ψ and f defined in the 2D (r, z) -plane. In view of our finite-element-based discretizations to be introduced below, we further define the 2D planar gradient and perpendicular operators according to

$$\nabla = \left(\frac{\partial}{\partial r}, \frac{\partial}{\partial z} \right)^T, \quad (A_r, A_z)^\perp = (-A_z, A_r), \quad \nabla^\perp = \left(-\frac{\partial}{\partial z}, \frac{\partial}{\partial r} \right)^T, \quad (8)$$

which we can also use to rewrite the terms in (5) as

$$\nabla_c \times (A_\phi \mathbf{e}_\phi) \sim_\phi \frac{1}{r} \nabla^\perp \Psi(r, z), \quad \left(\frac{\partial A_r}{\partial z} - \frac{\partial A_z}{\partial r} \right) \mathbf{e}_\phi \sim_\phi \frac{1}{r} f(r, z). \quad (9)$$

Ψ is called the *poloidal flux function*, and $\frac{1}{r}\nabla^\perp\Psi(r, z)$ corresponds to the 2D vector component of \mathbf{B} embedded in the *poloidal* (r, z) -plane. In contrast, f is called the *toroidal field function*, and the scalar field f/r corresponds to the out-of- (r, z) -plane component of \mathbf{B} aligned with the *toroidal* ϕ -coordinate. Assuming the embedded 2D planar pressure and toroidal field function to be functions of Ψ , i.e., $p = p(\Psi(r, z))$ and $f = f(\Psi(r, z))$, the equilibrium equation (3) can then be written purely as an equation in $\Psi(r, z)$, which is called the *Grad-Shafranov (GS)* equation.

The equation is a PDE in (r, z) -space, and its domain is an extension of the vertical cross-section (i.e., poloidal plane) of a tokamak. It can be solved using classical PDE discretization techniques such as the finite element method, returning $\Psi(r, z)$ on a 2D computational mesh, as well as f and p as functions of Ψ on discrete points $\{\Psi_i\}_{i=0}^m$ along a 1D interval $[\Psi_{\min}, \Psi_{\max}]$. In practice, f and p can then be expressed directly on the 2D computational mesh as $f(P_{1D}(\Psi(r, z)))$ and $p(P_{1D}(\Psi(r, z)))$, where P_{1D} is an interpolator acting on $\{\Psi_i\}_{i=0}^m$.

In addition, we note that in view of the discussion below, the split of \mathbf{B} into a Ψ - and an f -dependent part as in (9) will be useful in the process of loading data from the 2D GS mesh into the 3D MHD mesh. The expression $\nabla_c \times (A_\phi \mathbf{e}_\phi)$ is a vector that lies purely within the (r, z) -plane, while $(\frac{\partial A_r}{\partial z} - \frac{\partial A_z}{\partial r}) \mathbf{e}_\phi$ points along the ϕ -direction.

Finally, for the remainder of this work, we focus on the more complex Lorentz force term $\mathbf{B} \times \mathbf{J}$ (relative to the pressure gradient term), and consider zero-beta equilibria

$$\beta = 0 \quad \rightarrow \quad \mathbf{B} \times \mathbf{J} = \mathbf{0}, \quad (10)$$

although we note that the discussion to follow can readily be extended to cases with $\beta > 0$.

2.2. 2D component-wise conversion of the magnetic potential to MHD quantities

For axisymmetric equilibria considered in this work, as described above, vector fields can be decomposed into a 2D vector component within the (r, z) poloidal plane, denoted here by the subscript “ p ”, and a 2D out-of-plane toroidal scalar component, denoted by the subscript “ t ”, which is also a function in (r, z) -coordinates. Using these relations, we can express the embedded poloidal and the toroidal components of the magnetic field \mathbf{B} within the 2D (r, z) -plane as

$$\mathbf{B}_p(r, z) := \frac{1}{r} \nabla^\perp \Psi, \quad (11a)$$

$$B_t(r, z) := \frac{f}{r}. \quad (11b)$$

Note that (11) implies that the magnetic field is divergence-free, since in the axisymmetric case the ϕ -component $B_\phi \sim_\phi f/r$ of \mathbf{B} is independent of the ϕ -coordinate, and therefore

$$\nabla_c \cdot \mathbf{B} = \frac{1}{r} \frac{\partial(r(B_p)_r)}{\partial r} + \frac{\partial(B_p)_z}{\partial z} \sim_\phi \frac{1}{r} \nabla \cdot (r\mathbf{B}_p) = \nabla \cdot \nabla^\perp \Psi = 0, \quad (12)$$

where $\nabla_c \cdot (\cdot)$ denotes the divergence in cylindrical coordinates, and where we substituted for the definition of (11a). We will revisit the divergence of the magnetic field in our discretizations below, and for this purpose define D_b in the 2D (r, z) -plane as

$$D_b = \frac{1}{r} \nabla \cdot (r\mathbf{B}_p). \quad (13)$$

Next to considering the magnetic field’s divergence computation, we will also consider the computation of the current density $\mathbf{J} = \nabla \times \mathbf{B}$, which is a good indicator of the accuracy of our procedure for loading from GS data to MHD data. In particular, if the discrete current density as an MHD function is noisy, then we can expect the same to hold true for the Lorentz force term $\mathbf{B} \times \mathbf{J}$, which appears in the MHD equilibrium. Being an axisymmetric vector field, we again decompose \mathbf{J} into a poloidal vector and toroidal scalar component, which can be easily computed in an analogous fashion to (5). This leads to axisymmetric fields that can be expressed in 2D (r, z) -coordinates as

$$\mathbf{J}_p = \frac{1}{r} \nabla^\perp (rB_t), \quad (14a)$$

$$J_t = -\nabla^\perp \cdot \mathbf{B}_p. \quad (14b)$$

Note that the current density's components can also be expressed directly as functions of Ψ and f given (11), which are

$$\mathbf{J}_p = \frac{1}{r} \nabla^\perp f, \quad (15a)$$

$$J_t = -\nabla \cdot \left(\frac{1}{r} \nabla \Psi \right). \quad (15b)$$

Finally, when comparing results of mapping from GS to MHD fields, we will consider the zero-beta force balance equation (10) as a validation metric, which is associated with the so-called force-free equilibrium [25]. Our previous work finds that such a force balance equilibrium is difficult to achieve in transient MHD codes [7], which motivates the current work.

Given the component-wise magnetic field and its corresponding current density, the poloidal and toroidal components of the Lorentz force are given in the 2D (r, z) -plane by

$$[\mathbf{B} \times \mathbf{J}]_p = -B_t \mathbf{J}_p^\perp + J_t \mathbf{B}_p^\perp, \quad (16a)$$

$$[\mathbf{B} \times \mathbf{J}]_t = \mathbf{B}_p \cdot \mathbf{J}_p^\perp. \quad (16b)$$

Note that the Lorentz force's components can also be expressed directly as functions of \mathbf{B}_p and B_t given (14), which leads to

$$[\mathbf{B} \times \mathbf{J}]_p = \frac{1}{r} B_t \nabla(r B_t) - (\nabla^\perp \cdot \mathbf{B}_p) \mathbf{B}_p^\perp, \quad (17a)$$

$$[\mathbf{B} \times \mathbf{J}]_t = -\frac{1}{r} (\mathbf{B}_p \cdot \nabla(r B_t)). \quad (17b)$$

A more detailed derivation for the component-wise magnetic field as a function of the magnetic vector potential, as well as the Lorentz force reconstruction is given in [Appendix A](#).

3. Finite element discretization

When mapping GS fields to MHD fields, we consider a suitable discrete representation of the magnetic field components (11). Ideally, this discrete representation should satisfy the discrete divergence-free condition (12) and ensure that the discrete toroidal and poloidal current density components, and consequently the Lorentz force, exhibit low levels of noise. From the GS solver, we assume 2D fields given in discrete finite element spaces

$$\Psi \in \mathbb{V}_\Psi(\mathcal{T}_{GS})_k, \quad f \in \mathbb{V}_f(\mathcal{T}_{GS})_l, \quad (18)$$

where \mathcal{T}_{GS} is the mesh used in the GS solver, and k, l denote the spaces' polynomial degrees. Analogously, we assume

$$\mathbf{B}_p \in \mathbb{V}_{\mathbf{B}_p}(\mathcal{T}_{2D})_m, \quad B_t \in \mathbb{V}_{B_t}(\mathcal{T}_{2D})_n, \quad (19)$$

and

$$\mathbf{J}_p \in \mathbb{V}_{\mathbf{J}_p}(\mathcal{T}_{2D})_m, \quad J_t \in \mathbb{V}_{J_t}(\mathcal{T}_{2D})_n, \quad (20)$$

where \mathcal{T}_{2D} denotes the 2D poloidal restriction of the mesh used in the MHD solver, and m, n denote the spaces' polynomial degrees. Note that here we assume axisymmetric meshes for MHD, given the axisymmetric initial magnetic field configuration from the GS solver.

3.1. Compatible finite element spaces

Here, we introduce compatible finite element spaces to be used for the magnetic field and current density fields. We first discuss 2D finite element spaces. Using 2D quadrilateral elements as an example, Figure 1 shows the lowest two orders of 2D compatible finite element spaces. The top-left shows the first-order continuous Galerkin (CG) space $CG(\mathcal{T}_{2D})_1$, where the basis functions are defined on vertices. The gradient of a scalar defined in this CG space results in vectors naturally lying on cell edges, which corresponds to the curl-conforming space $H(\text{curl}, \mathcal{T}_{2D})_1$, while applying the gradient with a 90° rotation – that is ∇^\perp defined in (8) – results in vectors lying perpendicular to the edges, which corresponds to the divergence-conforming

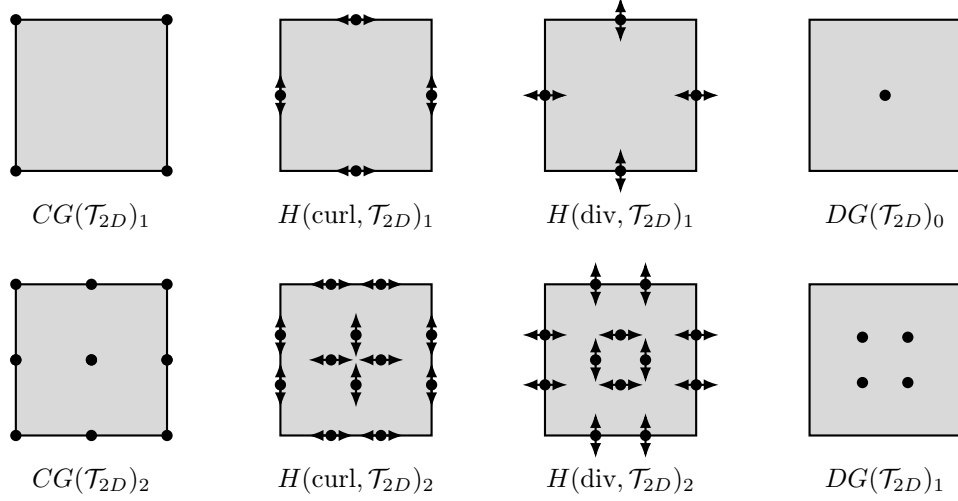


Figure 1: First-order and second-order continuous Galerkin spaces on a 2D quadrilateral element, along with their corresponding curl- and divergence-conforming spaces, and discontinuous Galerkin spaces.

space $H(\text{div}, \mathcal{T}_{2D})_1$. Finally, applying the divergence to vector fields defined in the $H(\text{div}, \mathcal{T}_{2D})_1$ space, or alternatively the divergence with a 90° rotation to vector fields defined in the $H(\text{curl}, \mathcal{T}_{2D})_1$ space, results in scalars lying in the zeroth-order discontinuous Galerkin (DG) space $DG(\mathcal{T}_{2D})_0$. The second row shows the second-lowest order of 2D compatible finite element spaces, with similar relationships with respect to the differential operators. The curl- and divergence-conforming spaces considered in this work are given by the Raviart-Thomas spaces RT_m^e , RT_m^f for triangles and RT_m^e , RT_m^f for quadrilaterals (as depicted in Figure 1).

Altogether, the 2D compatible finite element spaces can be seen in the context of a discrete de-Rham complex. That is, one space is mapped to another through differential operators, analogously to their non-discrete counterparts. The curl- and divergence-conforming 2D de-Rham complexes are given by

$$\begin{array}{ccccc}
 H^1(\Omega) & \xrightarrow{\nabla} & H(\text{curl}; \Omega) & \xrightarrow{\nabla^\perp} & L^2(\Omega) \\
 \downarrow \pi^0 & & \downarrow \pi^1 & & \downarrow \pi^2 \\
 \mathbb{V}_0(\Omega) & \xrightarrow{\nabla} & \mathbb{V}_1(\Omega) & \xrightarrow{\nabla^\perp} & \mathbb{V}_2(\Omega)
 \end{array}
 \quad
 \begin{array}{ccccc}
 H^1(\Omega) & \xrightarrow{\nabla^\perp} & H(\text{div}; \Omega) & \xrightarrow{\nabla} & L^2(\Omega) \\
 \downarrow \pi^0 & & \downarrow \pi^1 & & \downarrow \pi^2 \\
 \mathbb{V}_0(\Omega) & \xrightarrow{\nabla^\perp} & \mathbb{V}_1(\Omega) & \xrightarrow{\nabla} & \mathbb{V}_2(\Omega)
 \end{array}$$

respectively, for a 2D domain Ω , and where π^i denote projections from the Sobolev spaces to their discrete counterparts. $H^1(\Omega)$ corresponds to the $CG(\mathcal{T}_{2D})_m$ space, $H(\text{curl}; \Omega)$ to the $H(\text{curl}, \mathcal{T}_{2D})_m$ space, $H(\text{div}; \Omega)$ to the $H(\text{div}, \mathcal{T}_{2D})_m$ space and $L^2(\Omega)$ to the $DG(\mathcal{T}_{2D})_{m-1}$ space.

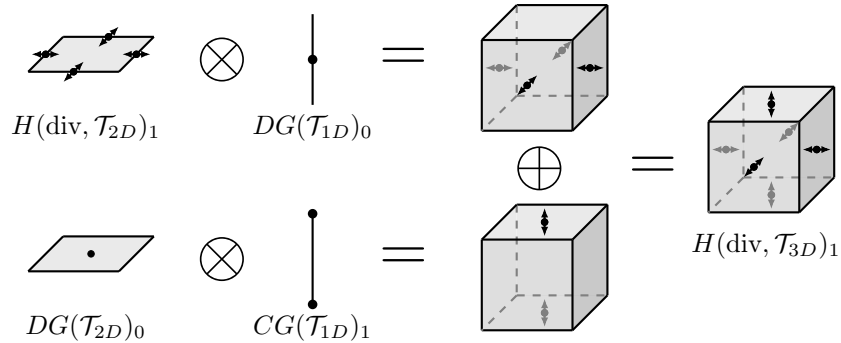


Figure 2: Illustration of forming 3D finite element spaces from tensor products of 1D finite element spaces and 2D finite element spaces, using the example of a 3D divergence-conforming space based on a 2D divergence-conforming space and a 2D DG space.

3D compatible finite element spaces can be obtained from tensor products between 1D compatible finite element spaces and 2D compatible finite element spaces [26]. For example, Figure 2 shows an illustration of $H(\text{div}, \mathcal{T}_{3D})_1$ formed as the sum of $H(\text{div}, \mathcal{T}_{2D})_1 \otimes DG(\mathcal{T}_{1D})_0$ and $DG(\mathcal{T}_{2D})_0 \otimes CG(\mathcal{T}_{1D})_1$, where \otimes denotes the tensor product of function spaces. We can similarly form other compatible finite element spaces in 3D, which are illustrated in Figure 3, where the lowest order compatible finite element spaces on a 3D hexahedral element are shown as an example.

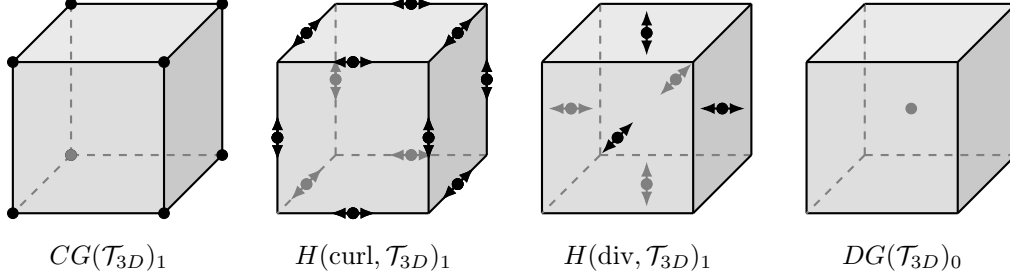


Figure 3: First-order continuous Galerkin space on a 3D hexahedral element, along with its corresponding curl- and divergence-conforming spaces, and discontinuous Galerkin space.

One common choice of magnetic field space used to satisfy the divergence-free condition exactly (in a strong or weak form) is given by divergence- and curl-conforming finite element spaces. In the case of tokamak meshes whose edges are either contained exactly in an (r, z) -plane or aligned exactly along the ϕ -coordinate, these spaces can naturally be associated with a vector space $\mathbb{V}_{\mathbf{B}_p}$ and a scalar space \mathbb{V}_{B_t} in the 2D poloidal plane. This holds true since the degrees of freedom of these spaces are associated with edges and faces, and therefore, if edges and faces are aligned exactly with the (r, z) -plane or ϕ -direction, each degree of freedom can be associated exactly with either the poloidal plane or the (scalar) toroidal direction.

In light of the formation of 3D spaces from tensor products of 1D and 2D spaces, we can decompose a 3D vector finite element space into a 2D vector finite element space and a 2D scalar finite element space within the (r, z) -plane, and consider \mathbf{B}_p in the former and B_t in the latter space. For divergence-conforming magnetic fields, these two spaces are given by

$$\mathbf{B}(r, \phi, z) \in H(\text{div}, \mathcal{T}_{3D})_m \rightarrow \mathbb{V}_{\mathbf{B}_p} = H(\text{div}, \mathcal{T}_{2D})_m, \quad \mathbb{V}_{B_t} = DG(\mathcal{T}_{2D})_{m-1}, \quad (21)$$

where $H(\text{div}, \mathcal{T})_m$ denotes a divergence-conforming space of polynomial order m defined on a mesh \mathcal{T} , and $DG(\mathcal{T}_{2D})_{m-1}$ denotes the DG space appearing in the same de-Rham complex as the divergence-conforming space (see Figure 2). On the other hand, for curl-conforming magnetic fields, the spaces are given by

$$\mathbf{B}(r, \phi, z) \in H(\text{curl}, \mathcal{T}_{3D})_m \rightarrow \mathbb{V}_{\mathbf{B}_p} = H(\text{curl}, \mathcal{T}_{2D})_m, \quad \mathbb{V}_{B_t} = CG(\mathcal{T}_{2D})_m, \quad (22)$$

where $H(\text{curl}, \mathcal{T})_m$ is defined analogously to the divergence-conforming version, and $CG(\mathcal{T}_{2D})_m$ denotes a CG space of the same de-Rham complex. Similarly for the divergence-conforming current density fields, we have

$$\mathbf{J}(r, \phi, z) \in H(\text{div}, \mathcal{T}_{3D})_m \rightarrow \mathbb{V}_{\mathbf{J}_p} = H(\text{div}, \mathcal{T}_{2D})_m, \quad \mathbb{V}_{J_t} = DG(\mathcal{T}_{2D})_{m-1}, \quad (23)$$

and for the curl-conforming current density fields, we have

$$\mathbf{J}(r, \phi, z) \in H(\text{curl}, \mathcal{T}_{3D})_m \rightarrow \mathbb{V}_{\mathbf{J}_p} = H(\text{curl}, \mathcal{T}_{2D})_m, \quad \mathbb{V}_{J_t} = CG(\mathcal{T}_{2D})_m. \quad (24)$$

3.2. Vector-CG spaces

Besides the compatible finite element spaces, another choice of finite element spaces for vector fields in MHD is given by vector-CG spaces (e.g., [6]). While such spaces are simpler to construct than divergence- and curl-conforming finite element spaces, the resulting MHD discretizations generally require divergence-cleaning methods since the resulting discrete magnetic field evolution in time will generally not be naturally divergence-free. These spaces are defined as $CG(\mathcal{T}_{2D})_m^d$, where the degree m is the polynomial degree of the finite element space and d is the dimension of the vector field. Under vector-CG spaces, for the special case

of MHD discretizations in (r, ϕ, z) -coordinates³, as well as for poloidal planes that lie on the x - or y -axis for MHD discretizations in (x, y, z) -coordinates, the magnetic field \mathbf{B} can again be decomposed as

$$\mathbf{B}(r, \phi, z) \in CG(\mathcal{T}_{2D})_m^3 \rightarrow \mathbb{V}_{\mathbf{B}_p} = CG(\mathcal{T}_{2D})_m^2, \quad \mathbb{V}_{B_t} = CG(\mathcal{T}_{2D})_m, \quad (25)$$

while the current density \mathbf{J} is decomposed as

$$\mathbf{J}(r, \phi, z) \in CG(\mathcal{T}_{2D})_m^3 \rightarrow \mathbb{V}_{\mathbf{J}_p} = CG(\mathcal{T}_{2D})_m^2, \quad \mathbb{V}_{J_t} = CG(\mathcal{T}_{2D})_m. \quad (26)$$

4. Numerical discretization

4.1. Discretization of the magnetic field

In light of the definitions of \mathbf{B}_p and B_t given in (11), we next describe the magnetic fields' discrete derivations given the choice of finite element spaces for the scalar fields Ψ and f .

If Ψ is a CG field, then according to the 2D de-Rham complex in the (r, z) -plane, \mathbf{B}_p should be divergence-conforming, and computed from (11a) as

$$\langle \mathbf{w}, r\mathbf{B}_p - \nabla^\perp \Psi \rangle = 0, \quad \forall \mathbf{w} \in H(\text{div}, \mathcal{T}_{2D})_m, \quad (27)$$

since $\nabla^\perp \Psi \in H(\text{div}, \mathcal{T}_{2D})_m$. Here, $\langle \cdot, \cdot \rangle$ denotes the L^2 -inner product. Note that the derivation of \mathbf{B}_p only holds weakly due to the additional factor of r arising from the Jacobian in cylindrical coordinates. In contrast, if Ψ is a DG field, then in an analogous argument, \mathbf{B}_p should be curl-conforming, and computed weakly as

$$\langle \Sigma, r\mathbf{B}_p \rangle + \langle \nabla^\perp \cdot \Sigma, \Psi \rangle - \int_{\partial \mathcal{T}_{2D}} \Psi(\Sigma \cdot \mathbf{n}^\perp) dS = 0, \quad \forall \Sigma \in H(\text{curl}, \mathcal{T}_{2D})_m, \quad (28)$$

where we used integration by parts (for further details, see Appendix B). Here, we note that finite element-based GS solvers typically do not return Ψ as a DG field. However, in this case we may still compute \mathbf{B}_p in the $H(\text{curl}, \mathcal{T}_{2D})_m$ space using (28). The pairing of Ψ with the DG field $\nabla^\perp \cdot \Sigma$ (noting the 2D planar de-Rham complex) then implicitly corresponds to projecting Ψ into the DG space.

For the toroidal component B_t , if f is a CG field, then B_t also naturally corresponds to a CG field, computed as

$$\langle \eta, rB_t - f \rangle = 0, \quad \forall \eta \in CG(\mathcal{T}_{2D})_m, \quad (29)$$

while if f is a DG field, then similarly B_t should be a DG field, computed as

$$\langle \phi, rB_t - f \rangle = 0, \quad \forall \phi \in DG(\mathcal{T}_{2D})_{m-1}. \quad (30)$$

Again, we note that f is generally not returned as a DG field in GS solvers, and we may still consider (30) to compute B_t for CG fields f .

Besides compatible finite element spaces, we also consider vector-CG spaces for comparison. If Ψ is a CG field, then \mathbf{B}_p should be in a 2D vector-CG space, and computed as

$$\langle \mathbf{v}, r\mathbf{B}_p - \nabla^\perp \Psi \rangle = 0, \quad \forall \mathbf{v} \in CG(\mathcal{T}_{2D})_m^2. \quad (31)$$

The toroidal component B_t should lie in a 2D scalar CG space, which is already given in (29).

Note that at this point, we have not specified the degree m yet. In practice, the degree may, for example, be set according to the position of the Ψ -finite element space within the de-Rham complex. For instance, if $\Psi \in CG(\mathcal{T}_{2D})_k$, then we would consider a divergence-conforming poloidal magnetic field \mathbf{B}_p set in $H(\text{div}, \mathcal{T}_{2D})_k$ (assuming Raviart-Thomas spaces). If $\Psi \in DG(\mathcal{T}_{2D})_k$, then we would instead consider a curl-conforming field \mathbf{B}_p set in $H(\text{curl}, \mathcal{T}_{2D})_{k+1}$. Note, however, that the best choice of degree may change given the additional factor of r in the above equations.

³In practice, finite element discretizations for non-reduced MHD systems are considered in (x, y, z) -coordinates, since coordinate transformations are handled automatically within the finite element reference-cell transformation. However, e.g., finite difference discretizations are typically posed in (r, ϕ, z) -coordinates for easier meshing, and in the case of collocated such discretizations, the GS-to-MHD data transfer in (r, ϕ, z) -coordinates can equivalently be represented using vector-CG spaces.

4.2. Discretization of the divergence of the magnetic field

Further, given the above definitions of computing \mathbf{B}_p in cylindrical coordinates, the curl-conforming version can be shown to be weakly divergence-free.

Proposition 4.1. *Let $\mathbf{B}_p \in H(\text{curl}, \mathcal{T}_{2D})_m$ be defined by (28). Further, assume the boundary of our 2D planar domain to be piecewise linear. Then \mathbf{B}_p admits as discrete divergence $D_b \in CG(\mathcal{T}_{2D})_m$ such that $D_b \equiv 0$.*

Proof. We define a discrete weak divergence D_b as

$$\langle \eta, rD_b \rangle = -\langle r\nabla\eta, \mathbf{B}_p \rangle + \int_{\partial\mathcal{T}_{2D}} r\eta g_1 dS, \quad \forall \eta \in CG(\mathcal{T}_{2D})_m, \quad (32)$$

for

$$g_1 := -\frac{1}{r} \mathbf{n} \cdot \nabla^\perp \Psi. \quad (33)$$

Since η is a CG test function, we have that $\nabla\eta$ is a curl-conforming function, and we can substitute for (28) with Σ set to $\nabla\eta$. This then leads to

$$\langle \eta, rD_b \rangle = -\langle \nabla^\perp \cdot \nabla\eta, \Psi \rangle + \int_{\partial\mathcal{T}_{2D}} \Psi(\nabla\eta \cdot \mathbf{n}^\perp) dS + \int_{\partial\mathcal{T}_{2D}} r\eta g_1 dS, \quad \forall \eta \in CG(\mathcal{T}_{2D})_m. \quad (34)$$

We then use the discrete identity $\nabla^\perp \cdot \nabla\eta = 0$, such that the first term on the right-hand side vanishes. Further, since we assume a piecewise linear boundary, it can be shown that $\nabla \cdot \mathbf{n}^\perp = 0$ along $\partial\mathcal{T}_{2D}$, and upon applying integration by parts for the first term on the right-hand side (along $\partial\mathcal{T}_{2D}$), we find that the last two terms cancel. \square

Note that using the definition of \mathbf{B}_p , the term g_1 corresponds to $-\mathbf{n} \cdot \mathbf{B}_p$. This is as expected, as can be seen from taking the inner product of the divergence's strong form (13) with a test function η and integrating the divergence of \mathbf{B}_p by parts. In particular, this also implies that our weak definition (32) is consistent with the divergence's strong form.

While the curl-conforming discrete version of \mathbf{B}_p is (weakly) divergence-free, this property no longer holds true for the divergence-conforming version. This is because in strong form (11a), we can directly apply the axisymmetric cylindrical coordinate divergence operator $\nabla_c \cdot (\cdot) = \frac{1}{r} \nabla \cdot (r(\cdot))$, while in weak form (27) – which is required due to the factor of r – such a direct application is no longer possible. In practice, a divergence cleaning operation may therefore be necessary for divergence-conforming \mathbf{B}_p .

To verify how the different discretizations preserve the divergence-free property, we will compute the divergence of the magnetic field in both divergence- and curl-conforming finite element spaces and in vector-CG spaces. If \mathbf{B}_p is divergence-conforming, the divergence D_b in DG is discretely computed as

$$\langle r\phi, D_b - \frac{1}{r} \nabla \cdot (r\mathbf{B}_p) \rangle = 0, \quad \forall \phi \in DG(\mathcal{T}_{2D})_{m-1}, \quad (35)$$

while if \mathbf{B}_p is curl-conforming, the divergence D_b in CG is discretely computed as

$$\langle \eta, rD_b \rangle = -\langle r\nabla\eta, \mathbf{B}_p \rangle + \int_{\partial\mathcal{T}_{2D}} r\eta g_1 dS, \quad \forall \eta \in CG(\mathcal{T}_{2D})_m. \quad (36)$$

In the vector-CG case, we can compute the divergence D_b in CG as

$$\langle r\eta, D_b - \frac{1}{r} \nabla \cdot (r\mathbf{B}_p) \rangle = 0, \quad \forall \eta \in CG(\mathcal{T}_{2D})_m. \quad (37)$$

4.3. Discretization of the current density field

Given the discrete magnetic field, the choice of divergence- or curl-conforming finite element space or vector-CG space also determines the choice of space for the current density. If \mathbf{B} is divergence-conforming, then \mathbf{J} is naturally curl-conforming and vice versa. If \mathbf{B} is in a vector-CG space, then for simplicity we also

compute \mathbf{J} in a vector-CG space. In the following, we rely on our computed formulas for the current density, such as (14).

For the poloidal component of the current density \mathbf{J}_p , if B_t is in a CG space, then \mathbf{J}_p should be divergence-conforming and computed as

$$\langle \mathbf{w}, r\mathbf{J}_p - \nabla^\perp(rB_t) \rangle = 0, \quad \forall \mathbf{w} \in H(\text{div}, \mathcal{T}_{2D})_m. \quad (38)$$

Alternatively, if B_t is in a DG space, then \mathbf{J}_p should be curl-conforming and computed weakly as

$$\langle \boldsymbol{\Sigma}, r\mathbf{J}_p \rangle + \langle \nabla^\perp \cdot \boldsymbol{\Sigma}, rB_t \rangle - \int_{\partial\mathcal{T}_{2D}} rB_t(\boldsymbol{\Sigma} \cdot \mathbf{n}^\perp) dS = 0, \quad \forall \boldsymbol{\Sigma} \in H(\text{curl}, \mathcal{T}_{2D})_m. \quad (39)$$

For the toroidal component J_t , the choice of space similarly depends on the poloidal magnetic field \mathbf{B}_p . If \mathbf{B}_p is curl-conforming, then J_t should be in a DG space and computed as

$$\langle r\phi, J_t + \nabla \cdot \mathbf{B}_p^\perp \rangle = 0, \quad \forall \phi \in DG(\mathcal{T}_{2D})_{m-1}. \quad (40)$$

On the other hand, if \mathbf{B}_p is divergence-conforming, then J_t should be in a CG space and computed weakly as

$$\langle r\eta, J_t \rangle + \langle \nabla^\perp(r\eta), \mathbf{B}_p \rangle - \int_{\partial\mathcal{T}_{2D}} r\eta(\mathbf{B}_p \cdot \mathbf{n}^\perp) dS = 0, \quad \forall \eta \in CG(\mathcal{T}_{2D})_m. \quad (41)$$

In the vector-CG case, given B_t in a CG space, we can compute \mathbf{J}_p in 2D vector-CG space as

$$\langle \mathbf{w}, r\mathbf{J}_p - \nabla^\perp(rB_t) \rangle = 0, \quad \forall \mathbf{w} \in CG(\mathcal{T}_{2D})_m^2, \quad (42)$$

and given \mathbf{B}_p in 2D vector-CG space, we can compute J_t in a CG space as

$$\langle r\eta, J_t + \nabla \cdot \mathbf{B}_p^\perp \rangle = 0, \quad \forall \eta \in CG(\mathcal{T}_{2D})_m. \quad (43)$$

Next to this, we note that in principle, we can also discretize the direct current density equations (15). For instance, for CG fields f and Ψ , we would have divergence-conforming \mathbf{J}_p and J_t in a CG space defined by

$$\langle \mathbf{w}, r\mathbf{J}_p - \nabla^\perp f \rangle = 0, \quad \forall \mathbf{w} \in H(\text{div}, \mathcal{T}_{2D})_m, \quad (44a)$$

$$\langle \eta, rJ_t \rangle - \langle \nabla(r\eta), \frac{1}{r} \nabla \Psi \rangle + \int_{\partial\mathcal{T}_{2D}} \eta(\mathbf{n} \cdot \nabla \Psi) dS = 0, \quad \forall \eta \in CG(\mathcal{T}_{2D})_m. \quad (44b)$$

4.4. Discretization of the Lorentz force

When comparing the results, we will also consider the force balance equation (3) as the validation metric. The components of the Lorentz force terms $[\mathbf{B} \times \mathbf{J}]_p$ and $[\mathbf{B} \times \mathbf{J}]_t$ lie in the given MHD discretization's choice of velocity space, which is typically (but not always) set equal to the magnetic field space. Here, we follow this approach and set the Lorentz force components to be in the same space as the components of the magnetic field, \mathbf{B}_p and B_t , respectively. In other words, if \mathbf{B}_p is divergence-conforming, then we also consider $[\mathbf{B} \times \mathbf{J}]_p$ to be divergence-conforming,

$$\langle r\mathbf{w}, [\mathbf{B} \times \mathbf{J}]_p + B_t \mathbf{J}_p^\perp - J_t \mathbf{B}_p^\perp \rangle = 0, \quad \forall \mathbf{w} \in H(\text{div}, \mathcal{T}_{2D})_m. \quad (45)$$

If \mathbf{B}_p is curl-conforming, $[\mathbf{B} \times \mathbf{J}]_p$ can be computed in a similar way except that $[\mathbf{B} \times \mathbf{J}]_p$ should lie in $H(\text{curl}, \mathcal{T}_{2D})_m$.

If B_t is in a CG space, then $[\mathbf{B} \times \mathbf{J}]_t$ should be in a CG space, and computed as

$$\langle r\eta, [\mathbf{B} \times \mathbf{J}]_t - \mathbf{B}_p \cdot \mathbf{J}_p^\perp \rangle = 0, \quad \forall \eta \in CG(\mathcal{T}_{2D})_m. \quad (46)$$

If B_t is in DG, $[\mathbf{B} \times \mathbf{J}]_t$ can be computed in a similar way except that $[\mathbf{B} \times \mathbf{J}]_t$ should lie in $DG(\mathcal{T}_{2D})_{m-1}$.

Under the vector-CG spaces, we generally will not use \mathbf{J} as an auxiliary variable. Instead, we will compute the Lorentz force directly from the magnetic field \mathbf{B} by (17). The discretization of the Lorentz force, in this case, is given by

$$\left\langle r\mathbf{v}, [\mathbf{B} \times \mathbf{J}]_p - \frac{1}{r} B_t \nabla(rB_t) + (\nabla^\perp \cdot \mathbf{B}_p) \mathbf{B}_p^\perp \right\rangle = 0, \quad \forall \mathbf{v} \in CG(\mathcal{T}_{2D})_m^2, \quad (47a)$$

$$\left\langle r\eta, [\mathbf{B} \times \mathbf{J}]_t + \frac{1}{r} (\mathbf{B}_p \cdot \nabla(rB_t)) \right\rangle = 0, \quad \forall \eta \in CG(\mathcal{T}_{2D})_m. \quad (47b)$$

4.5. Cylindrical coordinate projections

In the above discussion, we found that the existing factors of r and $1/r$ interfere with the discrete de-Rham complex in (r, z) -coordinates, for example, rendering the divergence-conforming magnetic field no longer strictly divergence-free. They may also affect the accuracy of the MHD equilibrium; this can be seen for instance in the computation of J_t either directly from Ψ as in (44b), or indirectly via \mathbf{B}_p by first computing (27), followed by (41). These two routes are equivalent only in the absence of the factors of r and $1/r$. Further, all of the above equations may be divided by a factor of $1/r$ before formulating the weak variational form, which may be done for example, to cancel the Jacobian determinant factor of r arising in cylindrical coordinates. In practice, for example, the two computations for divergence-conforming \mathbf{B}_p given by

$$\langle \mathbf{w}, r\mathbf{B}_p - \nabla^\perp \Psi \rangle = 0, \quad \forall \mathbf{w} \in H(\text{div}, \mathcal{T}_{2D})_m, \quad (48a)$$

$$\langle \mathbf{w}, \mathbf{B}_p - \frac{1}{r} \nabla^\perp \Psi \rangle = 0, \quad \forall \mathbf{w} \in H(\text{div}, \mathcal{T}_{2D})_m, \quad (48b)$$

may lead to slightly different results depending on the choice of degree m . Similarly, the equations for curl-conforming \mathbf{B}_p (28) may also be given by

$$\langle \boldsymbol{\Sigma}, \mathbf{B}_p \rangle + \left\langle \nabla^\perp \cdot \left(\frac{1}{r} \boldsymbol{\Sigma} \right), \Psi \right\rangle - \int_{\partial \mathcal{T}_{2D}} \frac{\Psi}{r} (\boldsymbol{\Sigma} \cdot \mathbf{n}^\perp) dS = 0, \quad \forall \boldsymbol{\Sigma} \in H(\text{curl}, \mathcal{T}_{2D})_m. \quad (49)$$

This likewise holds true for the current density equations, like (39), which can alternatively be written as

$$\langle \boldsymbol{\Sigma}, \mathbf{J}_p \rangle + \left\langle \nabla^\perp \cdot \left(\frac{1}{r} \boldsymbol{\Sigma} \right), rB_t \right\rangle - \int_{\partial \mathcal{T}_{2D}} B_t (\boldsymbol{\Sigma} \cdot \mathbf{n}^\perp) dS = 0, \quad \forall \boldsymbol{\Sigma} \in H(\text{curl}, \mathcal{T}_{2D})_m, \quad (50)$$

and (44), which can alternatively be written as

$$\langle \mathbf{w}, \mathbf{J}_p - \frac{1}{r} \nabla^\perp f \rangle = 0, \quad \forall \mathbf{w} \in H(\text{div}, \mathcal{T}_{2D})_m, \quad (51a)$$

$$\langle \eta, J_t \rangle - \langle \nabla \eta, \frac{1}{r} \nabla \Psi \rangle + \int_{\partial \mathcal{T}_{2D}} \frac{1}{r} \eta (\mathbf{n} \cdot \nabla \Psi) dS = 0, \quad \forall \eta \in CG(\mathcal{T}_{2D})_m. \quad (51b)$$

However, in practice, the impact of the above choices is very minor. We have conducted numerical experiments confirming that the choice of using r or $1/r$ factors does not produce a noticeable difference in the presented results.

5. Implementation

Our implementation for projecting the GS fields onto the MHD fields is built on the C++ library MFEM [27]. The GS fields are obtained from a solver presented in [15], which is implemented in MFEM, with their values represented by MFEM grid functions. As mentioned earlier, we consider solutions where the GS solver enforces the condition $\nabla p = 0$. The GS solver provides $\Psi(r, z)$ as a first-order polynomial continuous Galerkin function, and defines $f = f(\Psi)$ as a linear function of $\Psi(r, z)$, which is then interpolated at the degree-of-freedom locations of Ψ . In other words, for this work, we assume

$$\Psi \in CG(\mathcal{T}_{GS})_1, \quad f \in CG(\mathcal{T}_{GS})_1. \quad (52)$$

Often, practical GS solutions, such as those from [11, 10], are stored and distributed as EFIT data with Ψ -values represented on a regular grid. For our purposes, such data can also be represented as a lowest-order CG field on a finite element mesh corresponding to the regular grid, and our discussion below holds equally true. Finally, we note that extensions to the GS solver from [15] to support higher polynomial order spaces and discontinuous Galerkin fields are currently under way, thereby allowing for greater flexibility with respect to our choices of function spaces discussed in Section 3.

In addition to considerations related to the GS solver used in this work, we also briefly discuss our meshing choices and implementation details related to MFEM.

5.1. Mesh

For the second and third sources of error mentioned in the introduction – that is, mesh-related factors – we examine the relation between the GS and MHD meshes \mathcal{T}_{GS} and \mathcal{T}_{2D} , respectively. Specifically, we consider three meshes for \mathcal{T}_{2D} , which are based on \mathcal{T}_{GS} ⁴: (i) the original GS mesh \mathcal{T}_{GS} as described in [15], which is given by an unstructured mesh with triangular elements; (ii) the GS mesh modified to contain a perturbation for each mesh node (r_i, z_i) given by

$$\begin{aligned} r'_i &= r_i + \alpha \sin(r_i), \\ z'_i &= z_i + \alpha \sin(z_i), \end{aligned} \quad (53)$$

with $\alpha = 0.05$, and (iii) the original GS mesh further refined along the separatrix. We note that in practice the misalignment between GS and MHD meshes is more significant. The second mesh is chosen to show even a small perturbation in the mesh can lead to large errors in the MHD fields.

The first and third meshes are shown in Figure 4, while the perturbed mesh is omitted as the perturbation is too small to be easily visually distinguishable from the original mesh. We first use the first mesh for both \mathcal{T}_{GS} and \mathcal{T}_{2D} , demonstrating the results under exact alignment. We then use the first mesh as \mathcal{T}_{GS} and the perturbed second mesh as \mathcal{T}_{2D} to analyze the effect of misalignment. Finally, to assess the impact of mesh refinement, we use the refined third mesh for both \mathcal{T}_{GS} and \mathcal{T}_{2D} , to examine the refinement's effectiveness in dealing with steep gradients near the separatrix.

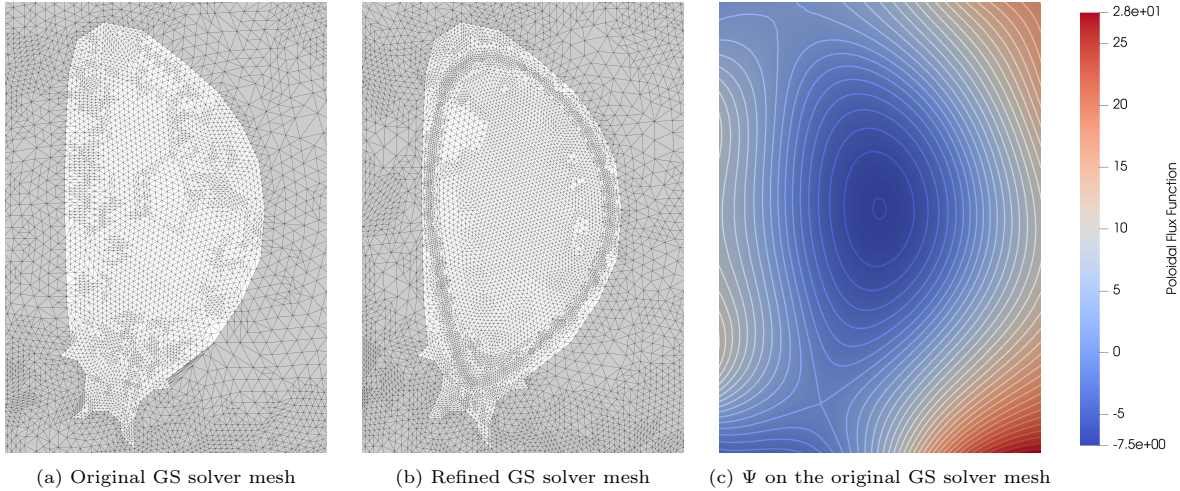


Figure 4: 2D meshes and input poloidal flux function used in the numerical experiments: (a) original GS solver mesh, (b) GS solver mesh with refinement along the separatrix, and (c) Ψ on the original GS solver mesh. The visualizations of the meshes are colored differently by the regions, of which the white region, which is inside the plasma-facing wall, is our MHD equilibrium's plasma region of interest.

5.2. Product rules

There are times when cylindrical coordinate projection coefficients cannot be separated from the test function, and therefore these terms cannot be implemented using the basic MFEM integrators. In these cases, we apply product rules to break a single term into two terms that can be computed with the basic integrators. For example, in (41), the r -coefficient cannot be separated from $\nabla^\perp(r\eta)$, and therefore, we apply product rule to obtain,

$$\begin{aligned} \langle \nabla^\perp(r\eta), \mathbf{B}_p \rangle &= \langle \eta \nabla^\perp r, \mathbf{B}_p \rangle + \langle r \nabla^\perp \eta, \mathbf{B}_p \rangle \\ &= \langle r \nabla^\perp \eta, \mathbf{B}_p \rangle + \langle \eta \mathbf{e}_z, \mathbf{B}_p \rangle, \quad \forall \eta \in CG(\mathcal{T}_{2D})_m. \end{aligned} \quad (54)$$

⁴Strictly speaking, the GS solver computes on a larger semi-circular cross-section that contains the tokamak reactor region. This domain includes regions that are not part of the MHD solver. In the numerical results considered here, we instead look into a rectangular mesh sub-section near the plasma region considered in the MHD solver. The mesh is identical to the original GS solver mesh within the plasma region, while the coils outside the plasma region are omitted.

Likewise, in (49), we apply product rule,

$$\begin{aligned} \left\langle \nabla^\perp \cdot \left(\frac{1}{r} \boldsymbol{\Sigma} \right), \Psi \right\rangle &= \left\langle \nabla^\perp \left(\frac{1}{r} \right) \cdot \boldsymbol{\Sigma}, \Psi \right\rangle + \left\langle \frac{1}{r} \nabla^\perp \cdot \boldsymbol{\Sigma}, \Psi \right\rangle \\ &= \left\langle -\frac{1}{r^2} \Sigma_r, \Psi \right\rangle + \left\langle \frac{1}{r} \nabla^\perp \cdot \boldsymbol{\Sigma}, \Psi \right\rangle, \quad \forall \boldsymbol{\Sigma} \in H(\text{curl}, \mathcal{T}_{2D})_m. \end{aligned} \quad (55)$$

5.3. Projection between misaligned meshes

When projecting between misaligned meshes, it is necessary to evaluate finite element grid functions at arbitrary spatial locations. To achieve this, we use the newly developed MFEM interface for GSLIB, which first locates the mesh element corresponding to the target point and then evaluates the polynomial basis functions at that location.

Further, to examine the impact of mesh misalignment, we adopt two projection methods depending on whether the field is computed weakly or strongly. For fields that are strongly computed, such as (27), we introduce auxiliary variables $\Psi \in CG(\mathcal{T}_{2D})_m$ and $f \in CG(\mathcal{T}_{2D})_m$, which are computed via L^2 projections from $\Psi \in CG(\mathcal{T}_{GS})_m$ and $f \in CG(\mathcal{T}_{GS})_m$, respectively. The inner products in the L^2 projections are r -weighted due to the Jacobian determinant factor from cylindrical coordinates. In contrast, the introduction of auxiliary variables is not needed for weak computations, such as (28), as Ψ and f appear directly in the right-hand side. In this case, we directly evaluate their values at the quadrature points on grid functions defined in $CG(\mathcal{T}_{GS})_m$.

Reproducibility. All implementation and numerical tests, including the projection approaches mentioned above, are available in the `tds-load` branch of MFEM at <https://github.com/mfem/mfem/tree/tds-load>. During our implementation process, the MFEM version was updated to version 4.6.

6. Numerical results

In this section, we present numerical results demonstrating the influence of the three error sources discussed above. First, we examine the effects of different finite element space choices. Next, we analyze the impact of mesh misalignment. Finally, we investigate the influence of mesh refinement along the separatrix as a way to reduce errors introduced by possibly under-resolved strong gradients near the separatrix.

6.1. Choice of finite element spaces

First, to focus on the error induced by the choice of finite element spaces, we begin by using the same mesh for both the MHD and GS solvers. As discussed in Section 5, finite element-based GS solvers typically return Ψ as a function in $CG(\mathcal{T}_{GS})_1$. The field $f = f(\Psi(r, z))$ (as well as the pressure p) is then given as a function of Ψ , which, after interpolation at the degree-of-freedom locations, also lies in $CG(\mathcal{T}_{GS})_1$.

Given these spaces for Ψ and f , and following our discussion on compatible finite element spaces in Section 4, a natural choice for the magnetic field is to place the poloidal component \mathbf{B}_p in $H(\text{div}, \mathcal{T}_{2D})_m$ and the toroidal component B_t in $CG(\mathcal{T}_{2D})_m$. The corresponding current density spaces then follow as \mathbf{J}_p in $H(\text{curl}, \mathcal{T}_{2D})_m$ and J_t in $CG(\mathcal{T}_{2D})_m$. Altogether, this leads to the following projections:

$$\begin{aligned} \Psi \in CG(\mathcal{T}_{2D})_m &\rightarrow \mathbf{B}_p \in H(\text{div}, \mathcal{T}_{2D})_m \rightarrow J_t \in CG(\mathcal{T}_{2D})_m, \\ f \in CG(\mathcal{T}_{2D})_m &\rightarrow B_t \in CG(\mathcal{T}_{2D})_m \rightarrow \mathbf{J}_p \in H(\text{div}, \mathcal{T}_{2D})_m, \end{aligned} \quad (56)$$

where we set $m = 1$ in view of the first-order polynomial functions Ψ and f returned by the GS solver.

However, as discussed in Section 3, the above choice of spaces does not naturally follow from a point of view of loading to 3D MHD fields. From (21)–(24), we have shown that a poloidal component in $H(\text{div}, \mathcal{T}_{2D})_m$ is naturally compatible with a toroidal component in $DG(\mathcal{T}_{2D})_{m-1}$ when constructing 3D finite element spaces from 2D ones via tensor products, while a poloidal component in $H(\text{curl}, \mathcal{T}_{2D})_m$ is naturally compatible with a toroidal component in $CG(\mathcal{T}_{2D})_m$. With this in mind, we can consider two alternative projection paths.

The first projection path is to put B_t in $DG(\mathcal{T}_{2D})_{m-1}$, and correspondingly \mathbf{J}_p in $H(\text{curl}, \mathcal{T}_{2D})_m$ in view of the 2D compatible finite element chain. This leads to the following projections:

$$\begin{aligned} \Psi \in CG(\mathcal{T}_{2D})_m &\xrightarrow{(27)} \mathbf{B}_p \in H(\text{div}, \mathcal{T}_{2D})_m \xrightarrow{(41)} J_t \in CG(\mathcal{T}_{2D})_m, \\ f \in CG(\mathcal{T}_{2D})_m &\xrightarrow{(30)} B_t \in DG(\mathcal{T}_{2D})_{m-1} \xrightarrow{(39)} \mathbf{J}_p \in H(\text{curl}, \mathcal{T}_{2D})_m, \end{aligned} \quad (57)$$

where we included equation numbers for the corresponding finite element computations from Section 4. The other alternative projection path in view of our 3D tensor products is to instead project \mathbf{B}_p into $H(\text{curl}, \mathcal{T}_{2D})_m$ and keep B_t in $CG(\mathcal{T}_{2D})_m$. This in turn leads to the following projections:

$$\begin{aligned} \Psi \in CG(\mathcal{T}_{2D})_m &\xrightarrow{(28)} \mathbf{B}_p \in H(\text{curl}, \mathcal{T}_{2D})_m \xrightarrow{(40)} J_t \in DG(\mathcal{T}_{2D})_{m-1}, \\ f \in CG(\mathcal{T}_{2D})_m &\xrightarrow{(29)} B_t \in CG(\mathcal{T}_{2D})_m \xrightarrow{(38)} \mathbf{J}_p \in H(\text{div}, \mathcal{T}_{2D})_m, \end{aligned} \quad (58)$$

where again we included the corresponding finite element computations' equation numbers.

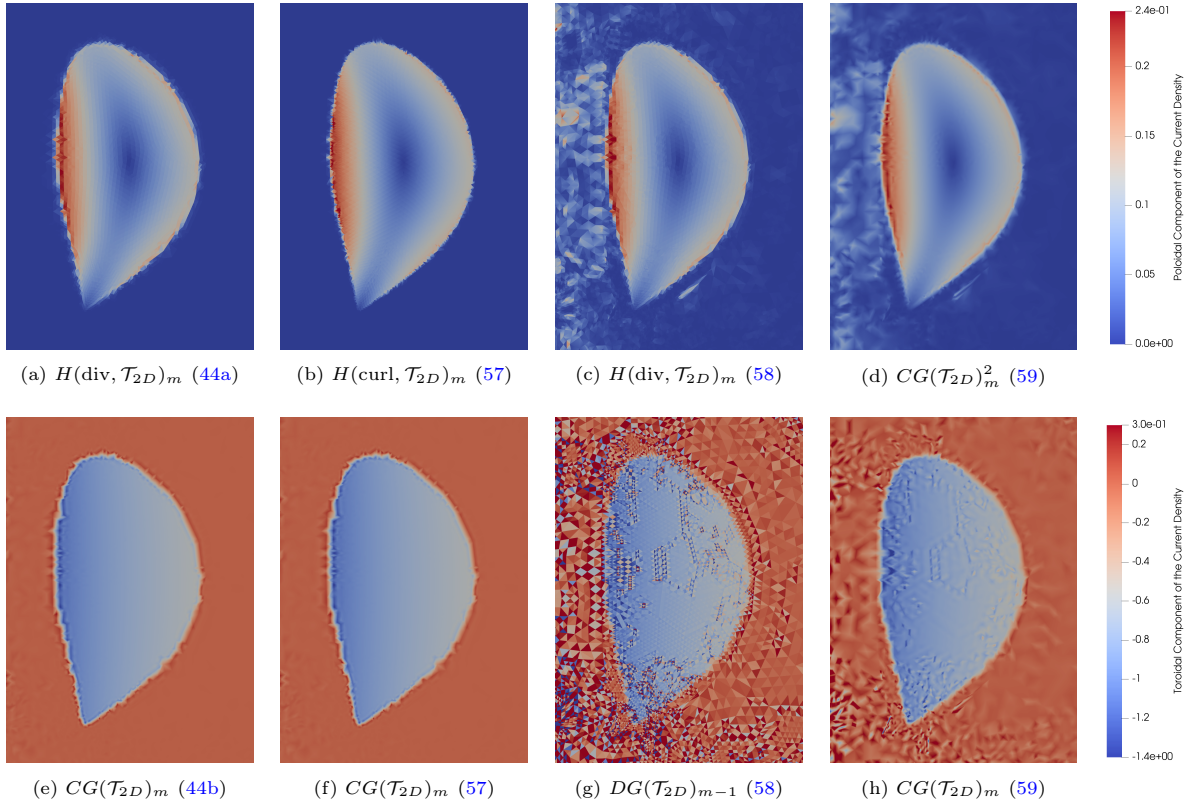


Figure 5: Comparison of the current density from different projection paths, for $\Psi, f \in CG(\mathcal{T}_{2D})_m$ and $m = 1$. Top row: Magnitude of poloidal component \mathbf{J}_p . (a) reference $\mathbf{J}_p \in H(\text{div}, \mathcal{T}_{2D})_m$ from (44a), (b) $\mathbf{J}_p \in H(\text{curl}, \mathcal{T}_{2D})_m$ from (57), (c) $\mathbf{J}_p \in H(\text{div}, \mathcal{T}_{2D})_m$ from (58), (d) $\mathbf{J}_p \in CG(\mathcal{T}_{2D})_m^2$ from (59). Bottom row: Toroidal component J_t . (e) reference $J_t \in CG(\mathcal{T}_{2D})_m$ from (44b), (f) $J_t \in CG(\mathcal{T}_{2D})_m$ from (57), (g) $J_t \in DG(\mathcal{T}_{2D})_{m-1}$ from (58), (h) $J_t \in CG(\mathcal{T}_{2D})_m$ from (59).

Besides the projection paths based on compatible finite element spaces, we also consider a setup based on vector-CG spaces. Under this setup, \mathbf{B}_p and \mathbf{J}_p are both in $CG(\mathcal{T}_{2D})_m^2$ and B_t and J_t are both in $CG(\mathcal{T}_{2D})_m$. This leads to the following projections:

$$\begin{aligned} \Psi \in CG(\mathcal{T}_{2D})_m &\xrightarrow{(31)} \mathbf{B}_p \in CG(\mathcal{T}_{2D})_m^2 \xrightarrow{(43)} J_t \in CG(\mathcal{T}_{2D})_m, \\ f \in CG(\mathcal{T}_{2D})_m &\xrightarrow{(29)} B_t \in CG(\mathcal{T}_{2D})_m \xrightarrow{(42)} \mathbf{J}_p \in CG(\mathcal{T}_{2D})_m^2, \end{aligned} \quad (59)$$

where all differential operations are computed strongly using, e.g., (42) and (43) for the current density's components.

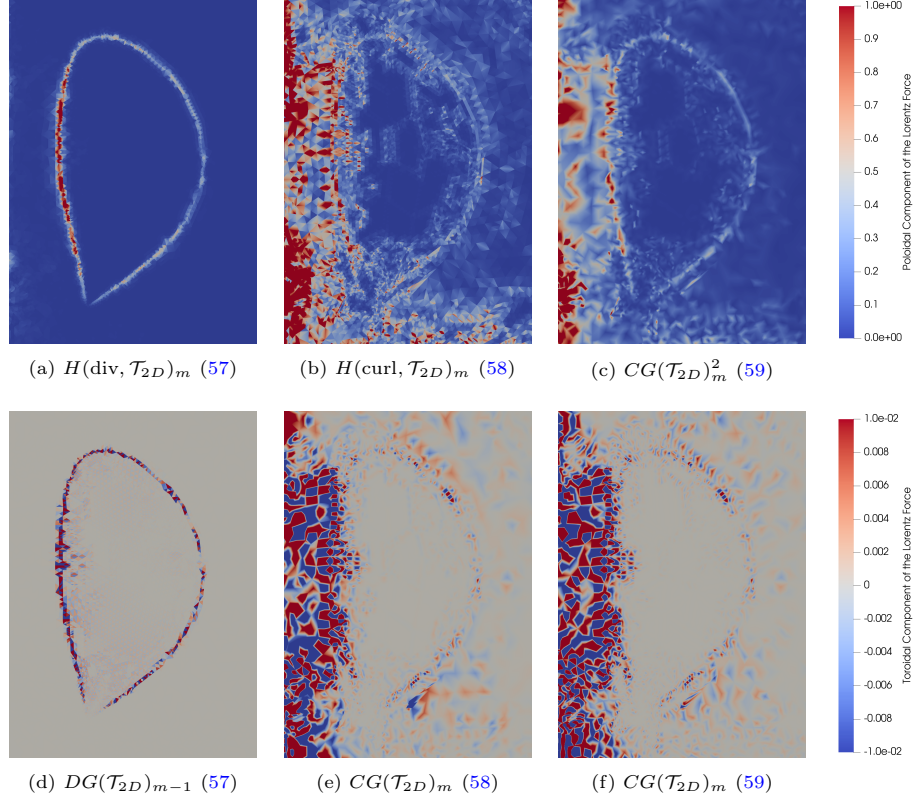


Figure 6: Comparison of the Lorentz force $[\mathbf{B} \times \mathbf{J}]$ from different projection paths into the corresponding poloidal and toroidal velocity spaces $\mathbb{V}_p, \mathbb{V}_t$, respectively. Top row: Poloidal component $[\mathbf{B} \times \mathbf{J}]_p$. (a) $\mathbb{V}_p = H(\text{div}, \mathcal{T}_{2D})_m$ from (57), (b) $\mathbb{V}_p = H(\text{curl}, \mathcal{T}_{2D})_m$ from (58), (c) $\mathbb{V}_p = CG(\mathcal{T}_{2D})_m^2$ from (59). Bottom row: Toroidal component $[\mathbf{B} \times \mathbf{J}]_t$. (d) $\mathbb{V}_t = DG(\mathcal{T}_{2D})_{m-1}$ from (57), (e) $\mathbb{V}_t = CG(\mathcal{T}_{2D})_m$ from (58), (f) $\mathbb{V}_t = CG(\mathcal{T}_{2D})_m$ from (59).

We test these different paths considering GS solutions from [15], as shown in Figure 4c. First, the resulting magnetic fields do not show visually distinguishable differences and are shown in Appendix C. Second, we compare the current density fields obtained from the three projection paths, together with results from the direct computation (44) as a reference. Since computing \mathbf{J} directly from f and Ψ is not impacted by the discretization error involved in magnetic field projections, the results from (44) should naturally contain less error. Figure 5 shows the current density fields from the three projection paths and the reference results.

The first row depicts the poloidal component of the current density fields. Since there are two components, J_r and J_z in \mathbf{J}_p , we show the magnitude of the field. Within the plasma region (see Figure 4 for the plasma domain described by the separatrix), all three projection paths yield results that are similar and are in relatively good agreement with the reference. In contrast, near the wall region and beyond, the projection paths (58) and (59) exhibit considerable noise. This noise is less important since the equilibrium is not evolved within the walls, and a higher quality mesh within the wall region will likely attenuate this noise.

In contrast, the toroidal component of the current density fields reveals more substantial discrepancies among the three projection paths. The second row shows the toroidal component of the current density fields from the reference result and the three projection paths above. This time, projection paths (58) and (59) also exhibit significant noise within the plasma region, which cannot be trivially eliminated. In contrast, the results from projection path (57) closely match the reference solution and remain largely free of noise. In particular, (57) follows the correct compatible finite element chain for computing \mathbf{B}_p and J_t , using a strong perpendicular gradient to compute the divergence-conforming field \mathbf{B}_p from the CG field Ψ , and a weak perpendicular gradient to compute the CG field J_t from \mathbf{B}_p . On the other hand, such a compatible framework does not hold true for (58), in which Ψ is first implicitly projected into the DG space (within (28)) when computing the curl-conforming field \mathbf{B}_p . Similarly, the vector-CG based approach (59) does not follow a framework of compatible function spaces with respect to the involved differential operators. Overall,

this underlines the importance of a compatible choice of finite element spaces when computing the current density field as a diagnostic of the initial magnetic field \mathbf{B} in the context of MHD solvers.

We further verify our findings with the force balance equation (3). Since $\nabla p = 0$ in this test case, both the toroidal and poloidal components of the Lorentz force should be zero. Figure 6 shows the Lorentz force from the same three projection paths as considered for the current density. The first row shows the poloidal component. Again, we present the magnitude of $[\mathbf{B} \times \mathbf{J}]_p$ for better visualization. Similarly to our findings for the current density, the projection path (57) gives close-to-zero $[\mathbf{B} \times \mathbf{J}]_p$ magnitudes except for the regions close to the separatrix, while the projection paths (58) and (59) lead to significant noise in the entire domain, including parts of the plasma region away from the separatrix.

This is also evident in the toroidal component of the Lorentz force, shown in the second row. The projection path (58) results in significant noise while the projection path (57) contains much less noise in all regions except for the separatrix. Altogether, given these current density and Lorentz force results, the projection path (57) – which follows the compatible finite element framework for computations based on the CG field Ψ – clearly leads to the smallest error, which is confined to the separatrix region.

Although projection path (57) yields the least error in terms of force balance, projection path (58) may still be preferable in some cases, as projecting \mathbf{B}_p in $H(\text{curl}, \mathcal{T}_{2D})$ provides additional advantages in maintaining the divergence-free property of the magnetic field. This holds true especially if Ψ is provided by the GS solver as a DG field, in which case the Ψ -related computations in (58) also fully follow the compatible finite element framework, based on the weak magnetic field computation (28). In this work, we only have access to a GS solver that returns Ψ as a CG field, although upgrades to also support Ψ in DG are under way and we aim to also discuss corresponding GS-to-MHD field transfer results in future work. In particular, as shown in Figure 7, the divergence from \mathbf{B}_p in $H(\text{curl}, \mathcal{T}_{2D})$ computed as (32) through projection path (58) is negligible in the entire region (see also Figure D.11 in Appendix D), while the divergences from \mathbf{B}_p in $H(\text{div}, \mathcal{T}_{2D})$ and $CG(\mathcal{T}_{2D})_m^2$ from projection paths (57) and (59), respectively, contain significant noise throughout the domain.

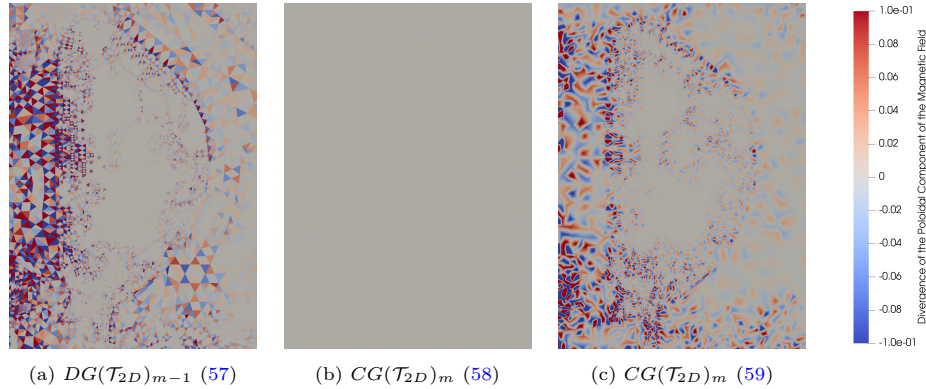


Figure 7: Comparison of the divergence of the poloidal component of the magnetic field (D_b) from different projection paths, with (D_b) in different spaces depending on the projection path. (a) $D_b \in DG(\mathcal{T}_{2D})_{m-1}$ from (57), (b) $D_b \in CG(\mathcal{T}_{2D})_m$ from (58), (c) $D_b \in CG(\mathcal{T}_{2D})_m$ from (59).

Therefore, given Ψ in CG, the natural choice is to compute \mathbf{B}_p in a divergence-conforming function space, which best eliminates the error induced by the implicit projection. This is verified by the force balance results above. However, divergence-conforming \mathbf{B}_p does not offer the additional advantage of maintaining the divergence-free property of the magnetic field. In order to minimize the error in both aspects, it is necessary to compute Ψ in DG from the GS solver so that we can obtain curl-conforming \mathbf{B}_p without additional errors introduced by the implicit projection of Ψ into DG.

6.2. Impact of mesh misalignment

We further analyze the impact of mesh misalignment on the numerical results, using the GS solver output from [15]. The comparison between the Lorentz force projected on the aligned mesh and the perturbed misaligned mesh is shown in Figure 8 (b, e). We show the results from projection path (57), which we showed above to be the path yielding the least noise in the aligned case. As expected and in line with

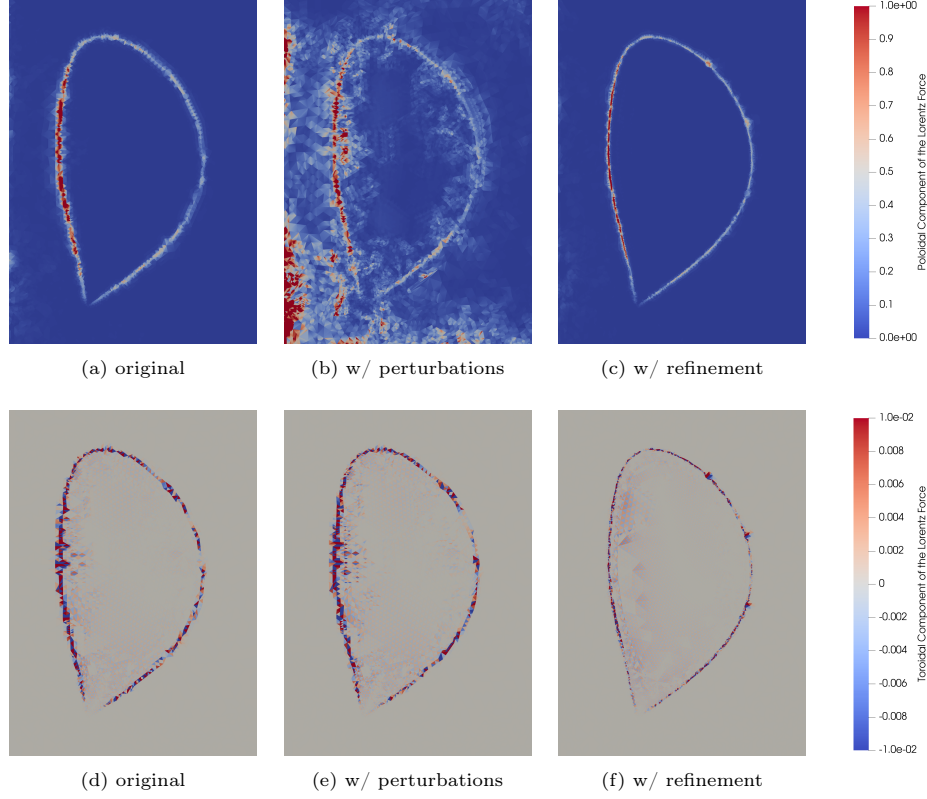


Figure 8: Comparison of the Lorentz force components from projection path (57). Top row: poloidal component $[\mathbf{B} \times \mathbf{J}]_p$. (a) original, (b) w/ perturbations, (c) w/ refinement. Bottom row: toroidal component $[\mathbf{B} \times \mathbf{J}]_t$. (e) original, (f) w/ perturbations, (g) w/ refinement.

previous observations in the literature, the results show that the misalignment leads to significant additional noise in the entire domain. In our case, we find this to be true especially in the poloidal component of the Lorentz force. In addition to the Lorentz force, we note that results for the divergence field are expected to be analogous in the non-mesh-aligned case to those in the aligned one. This holds true in particular for the weakly divergence-free projection path (58), which still leads to an approximately divergence-free magnetic field \mathbf{B} (see Appendix D). The reason behind this is that the divergence-free property relies on the identity $\nabla^\perp \cdot \nabla \equiv 0$ as well as a consistency condition of g_1 along the boundary (see Proposition 4.1), both of which hold true independently of the underlying choice of mesh.

6.3. Impact of mesh refinement

Finally, we analyze the impact of mesh refinement on the numerical results. In particular, we refine the mesh near the separatrix, which often contains steep gradients and also contains the main remaining error for the Lorentz force in our above results. This leverages one of the adaptivity strategies presented in our adaptive GS solver [15]. Figure 8 (c, f) shows the comparison between the Lorentz force computed on meshes with and without refinement. Again, we show the results from projection path (57). As expected, results show that refinement at the separatrix significantly reduces the error in all components of the Lorentz force.

Finally, we note that we have also conducted experiments on aligning mesh edges with the separatrix. Results indicate that such alignment does not further improve the accuracy as long as mesh refinement has been conducted along the separatrix. It is unclear why alignment with the separatrix does not lead to further improvements, and the final remaining error as seen in Figure 8 may be related to the projection of the CG field f into the DG field B_t within projection path (57). As mentioned before, in this work, we only have access to a GS solver that returns CG fields, including f . In future work, we aim to also discuss corresponding GS-to-MHD field transfer results in which f is a DG field, while retaining Ψ in DG (or vice versa), for fully compatible projection paths with divergence- or curl-conforming magnetic fields. We note

that our result does not contradict the practical popularity of field-aligned meshes used in transient MHD simulations in MCF. In recent studies [28, 29], the mesh alignment is found to be useful for anisotropic diffusion in MHD under a strong magnetic field.

7. Conclusion

In this work, we have studied the numerical errors involved in transferring GS equilibria to MHD solvers. We have identified several sources of such errors, including incompatibility between the finite element spaces used in the GS and MHD solvers, misalignment between the GS and MHD meshes, and possibly under-resolved strong gradients near the separatrix. We have derived several possible structure-preserving transferring strategies and have designed experiments to compare their numerical errors in terms of preserving the force balance and divergence-free properties of the magnetic field.

The incompatibility between the GS and MHD finite element spaces is examined within a compatible finite element framework. The compatible finite element framework implements a discretized de-Rham complex, where there is a natural choice of finite element space that corresponds to the differential operators involved in the projection path. To examine the incompatibility between the GS and MHD finite element spaces, we derive three candidate projection paths, among which two are compatible finite element space-based projection paths and one is based on vector-CG spaces, serving as a baseline. The numerical results show that the compatible finite element spaces perform significantly better than the vector-CG spaces in terms of MHD equilibrium errors and preserving the divergence-free property in the case of the curl-conforming magnetic field discretization. In particular, we find that given a GS solver output as a CG field, one of the proposed paths performs the best in terms of preserving the force balance, while the other path performs the best in terms of preserving the divergence-free property of the magnetic field, whereas the vector-CG spaces preserve neither property.

We have also examined the impact of mesh misalignment between the GS and MHD meshes. We experimented with this by applying a small perturbation to the MHD mesh. The numerical results show that a small perturbation to the MHD mesh is enough to result in large numerical errors in the force balance. This indicates that it is important to align the MHD mesh exactly with the GS mesh in order to minimize the force imbalance in the transferred equilibria. Finally, we have also examined the impact of the possibly under-resolved strong gradients near the separatrix on the numerical error. We find that mesh refinement along the separatrix is effective in reducing the numerical error in the force balance.

Overall, our results highlight that compatible finite element spaces offer significant advantages in minimizing the numerical errors involved in transferring GS equilibria to MHD solvers compared to e.g., vector-CG spaces. The choice of compatible finite element setup in turn requires suitable spaces returned by the GS solver, with Ψ in CG for divergence-conforming magnetic fields, and Ψ in DG for curl-conforming magnetic fields, yet divergence-conforming magnetic fields lose the divergence-free property. In future work, we aim to further test our projection path with curl-conforming magnetic fields that are naturally divergence-free, using an updated GS solver that can also provide Ψ as a DG field.

Appendix A. Derivation of component-wise field reconstructions in the 2D poloidal plane

Recall that we have defined $\nabla = (\frac{\partial}{\partial r}, \frac{\partial}{\partial z})^T$ and $(A_r, A_z)^\perp = (-A_z, A_r)$, and $\nabla_c \times (\cdot)$ denotes the curl in cylindrical coordinates. Thus, for an axisymmetric toroidal vector field $A_t \mathbf{e}_\phi = A_\phi \mathbf{e}_\phi$, we have

$$\nabla_c \times (A_t \mathbf{e}_\phi) = -\frac{\partial A_\phi}{\partial z} \mathbf{e}_r + \frac{1}{r} \frac{\partial(r A_\phi)}{\partial r} \mathbf{e}_z = \frac{1}{r} \left(-\frac{\partial(r A_\phi)}{\partial z} \mathbf{e}_r + \frac{\partial(r A_\phi)}{\partial r} \mathbf{e}_z \right) \sim_\phi \frac{1}{r} \nabla^\perp(r A_t), \quad (\text{A.1})$$

where A_t is the 2D embedding of A_ϕ into the (r, z) -plane. Further, for an axisymmetric poloidal vector field $\mathbf{A} = A_r \mathbf{e}_r + A_z \mathbf{e}_z$, we have

$$\nabla_c \times \mathbf{A} = \frac{1}{r} \frac{\partial A_z}{\partial \phi} \mathbf{e}_r + \left(\frac{\partial A_r}{\partial z} - \frac{\partial A_z}{\partial r} \right) \mathbf{e}_\phi - \frac{\partial A_r}{\partial \phi} \mathbf{e}_z = - \left(\frac{\partial A_z}{\partial r} - \frac{\partial A_r}{\partial z} \right) \mathbf{e}_\phi \sim_\phi - (\nabla^\perp \cdot \mathbf{A}_p), \quad (\text{A.2})$$

where \mathbf{A}_p is the component-wise 2D embedding of \mathbf{A} into the (r, z) -plane, noting that \mathbf{A} has no out-of-plane component. Note that we use the axisymmetry assumption here, such that $\frac{\partial A_z}{\partial \phi} = 0$ and $\frac{\partial A_r}{\partial \phi} = 0$.

For the Lorentz force components $[\mathbf{B} \times \mathbf{J}]_p$ and $[\mathbf{B} \times \mathbf{J}]_t$, we have

$$\begin{aligned}\mathbf{B} \times \mathbf{J} &= (B_r \mathbf{e}_r + B_\phi \mathbf{e}_\phi + B_z \mathbf{e}_z) \times (J_r \mathbf{e}_r + J_\phi \mathbf{e}_\phi + J_z \mathbf{e}_z) \\ &= (B_\phi J_z - B_z J_\phi) \mathbf{e}_r + (B_z J_r - B_r J_z) \mathbf{e}_\phi + (B_r J_\phi - B_\phi J_r) \mathbf{e}_z \\ &= -B_\phi (-J_z \mathbf{e}_r + J_r \mathbf{e}_z) + J_\phi (-B_z \mathbf{e}_r + B_r \mathbf{e}_z) + (-B_r J_z + B_z J_r) \mathbf{e}_\phi,\end{aligned}\quad (\text{A.3})$$

where the first two terms are the poloidal component and the third term is the toroidal component, that is

$$-B_\phi (-J_z \mathbf{e}_r + J_r \mathbf{e}_z) + J_\phi (-B_z \mathbf{e}_r + B_r \mathbf{e}_z) \sim_\phi (-B_t \mathbf{J}_p^\perp + J_t \mathbf{B}_p^\perp), \quad (\text{A.4})$$

$$(-B_r J_z + B_z J_r) \mathbf{e}_\phi \sim_\phi (\mathbf{B}_p \cdot \mathbf{J}_p^\perp). \quad (\text{A.5})$$

Thus, we have

$$[\mathbf{B} \times \mathbf{J}]_p = -B_t \mathbf{J}_p^\perp + J_t \mathbf{B}_p^\perp, \quad (\text{A.6})$$

$$[\mathbf{B} \times \mathbf{J}]_t = \mathbf{B}_p \cdot \mathbf{J}_p^\perp. \quad (\text{A.7})$$

Finally, we can derive $[\mathbf{B} \times \mathbf{J}]_p$ and $[\mathbf{B} \times \mathbf{J}]_t$ in terms of B_t and \mathbf{B}_p only, as

$$[\mathbf{B} \times \mathbf{J}]_p = -B_t \mathbf{J}_p^\perp + J_t \mathbf{B}_p^\perp = -B_t \left(\frac{1}{r} \nabla^\perp (r B_t) \right)^\perp - (\nabla^\perp \cdot \mathbf{B}_p) \mathbf{B}_p^\perp = \frac{1}{r} B_t \nabla (r B_t) - (\nabla^\perp \cdot \mathbf{B}_p) \mathbf{B}_p^\perp, \quad (\text{A.8})$$

and

$$[\mathbf{B} \times \mathbf{J}]_t = \mathbf{B}_p \cdot \mathbf{J}_p^\perp = \mathbf{B}_p \cdot \left(\frac{1}{r} \nabla^\perp (r B_t) \right)^\perp = -\frac{1}{r} (\mathbf{B}_p \cdot \nabla (r B_t)). \quad (\text{A.9})$$

Appendix B. Integration by parts for weak forms

Integration by parts was used to derive (28) from (11a). To see this, take the inner product of (11a) with a test function (before discretization, assuming suitably regular fields), and obtain

$$\langle \boldsymbol{\Sigma}, r \mathbf{B}_p \rangle = \langle \boldsymbol{\Sigma}, \nabla^\perp \Psi \rangle, \quad \forall \boldsymbol{\Sigma} \in H(\text{curl}, \mathcal{T}_{2D})_m, \quad (\text{B.1})$$

where we include an additional factor of r due to the Jacobian determinant when transforming the integration from cylindrical coordinates to the poloidal plane. We can then use the definition of the perpendicular operator (including its property $\mathbf{a}^\perp \cdot \mathbf{b} = -\mathbf{a} \cdot \mathbf{b}^\perp$ for any vectors \mathbf{a}, \mathbf{b}) together with integration by parts, which leads to

$$\langle \boldsymbol{\Sigma}, \nabla^\perp \Psi \rangle = -\langle \boldsymbol{\Sigma}^\perp, \nabla \Psi \rangle = \langle \nabla \cdot \boldsymbol{\Sigma}^\perp, \Psi \rangle - \int_{\partial \mathcal{T}_{2D}} \Psi (\boldsymbol{\Sigma}^\perp \cdot \mathbf{n}) dS = -\langle \nabla^\perp \cdot \boldsymbol{\Sigma}, \Psi \rangle + \int_{\partial \mathcal{T}_{2D}} (\boldsymbol{\Sigma} \cdot \mathbf{n}^\perp) dS. \quad (\text{B.2})$$

The weak computation of current density components can be derived in a similar manner.

Appendix C. Comparison of different projection paths for magnetic field

Figure C.9 shows the poloidal component of the magnetic field from the two projection paths. Since there are two components, B_r and B_z in \mathbf{B}_p , we show here the magnitude of the field. Overall there are no significant differences in the \mathbf{B}_p itself from the two projection paths, except for some minor differences that reveal the properties of different finite element spaces.

Figure C.10 shows the toroidal component of the magnetic field from the two projection paths. Similarly to the poloidal component, the results do not show significant differences except for the enforced smoothness of the toroidal component in the CG space.

Appendix D. Comparison of divergence of the poloidal component of the magnetic field under perturbations and refinement

Figure D.11 shows the divergence of the poloidal component of the magnetic field (D_b) from projection path (57) under mesh perturbations and refinement. Results show that neither perturbations nor refinement impact the divergence-free property of the poloidal magnetic field.

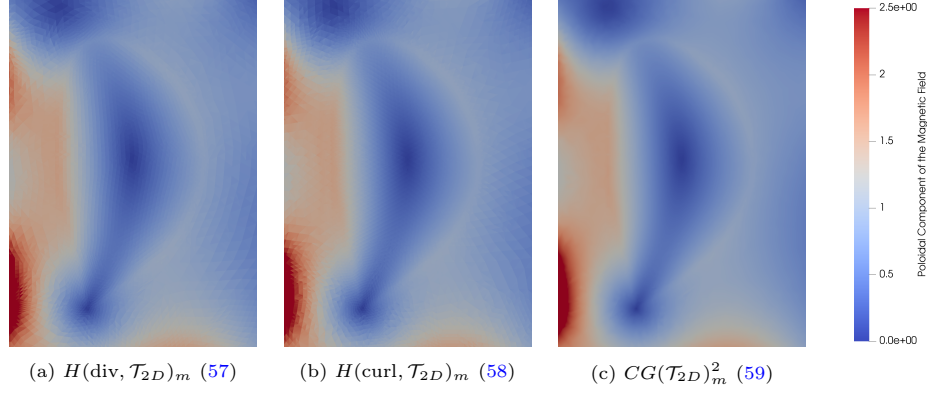


Figure C.9: Comparison of the poloidal component of the magnetic field B_p from different projection paths. (a) $H(\text{div}, \mathcal{T}_{2D})_m$ (57), (b) $H(\text{curl}, \mathcal{T}_{2D})_m$ (58), (c) $CG(\mathcal{T}_{2D})_m^2$ (59).

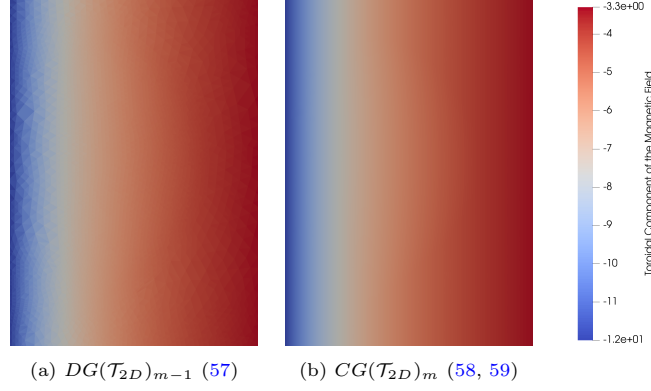


Figure C.10: Comparison of the toroidal component of the magnetic field B_t from different projection paths. (a) $DG(\mathcal{T}_{2D})_{m-1}$ (57), (b) $CG(\mathcal{T}_{2D})_m$ (58, 59).

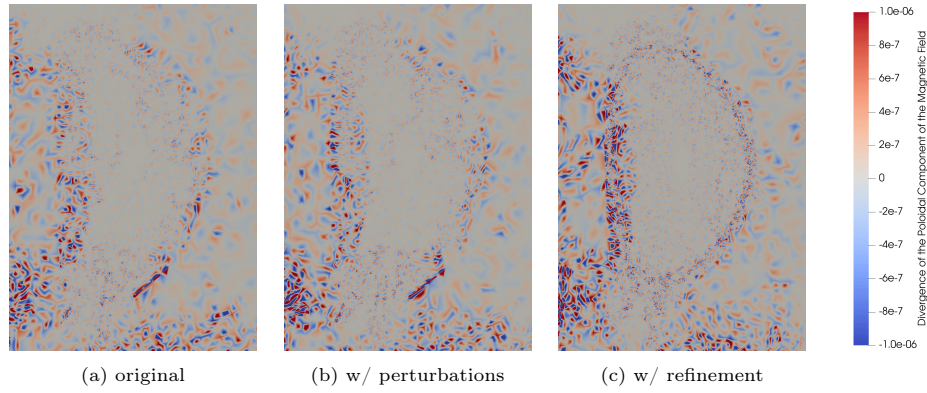


Figure D.11: Comparison of the divergence of the poloidal component of the magnetic field (D_b) from projection path (57). (a) original, (b) w/ perturbations, (c) w/ refinement.

References

- [1] S. Jardin, Computational methods in plasma physics, CRC press, 2010.
- [2] C. R. Sovinec, A. Glasser, T. Gianakon, D. Barnes, R. Nebel, S. Kruger, D. Schnack, S. Plimpton, A. Tarditi, M. Chu, et al., Nonlinear magnetohydrodynamics simulation using high-order finite elements, *Journal of Computational Physics* 195 (1) (2004) 355–386.
- [3] M. Hoelzl, G. T. Huijsmans, S. Pamela, M. Becoulet, E. Nardon, F. J. Artola, B. Nkonga, C. V. Atanasiu, V. Bandaru, A. Bhole, et al., The JOREK non-linear extended MHD code and applications to large-scale instabilities and their control in magnetically confined fusion plasmas, *Nuclear Fusion* 61 (6) (2021) 065001.
- [4] V. Igochine, et al., Active control of magneto-hydrodynamic instabilities in hot plasmas, Springer, 2015.
- [5] L. L. Lao, H. S. John, R. Stambaugh, A. Kellman, W. Pfeiffer, Reconstruction of current profile parameters and plasma shapes in tokamaks, *Nuclear fusion* 25 (11) (1985) 1611.
- [6] J. Bonilla, J. N. Shadid, X.-Z. Tang, M. M. Crockatt, P. Ohm, E. Phillips, R. Pawlowski, S. Conde, O. Beznosov, On a fully-implicit VMS-stabilized FE formulation for low Mach number compressible resistive MHD with application to MCF, *Computer Methods in Applied Mechanics and Engineering* 417 (2023) 116359.
- [7] Z. Jorti, Q. Tang, K. Lipnikov, X.-Z. Tang, A mimetic finite difference based quasi-static magneto-hydrodynamic solver for force-free plasmas in tokamak disruptions, *arXiv preprint arXiv:2303.08337* (2023).
- [8] J. Hamilton, L. Chacon, G. Keramidas, X.-Z. Tang, Aligning thermal and current quenches with a high density low-z injection, *arXiv preprint arXiv:2503.17557* (2025).
- [9] B. Dudson, FreeGS: Free boundary Grad-Shafranov solver, <https://github.com/freegs-plasma/freegs> (2024).
- [10] N. Amorisco, A. Agnello, G. Holt, M. Mars, J. Buchanan, S. Pamela, FreeGSNKE: A python-based dynamic free-boundary toroidal plasma equilibrium solver, *Physics of Plasmas* 31 (4) (2024).
- [11] S. Liu, Q. Tang, X.-Z. Tang, A parallel cut-cell algorithm for the free-boundary Grad-Shafranov problem, *SIAM Journal on Scientific Computing* 43 (6) (2021) B1198–B1225.
- [12] A. Farmakalides, N. Nikiforakis, S. Millmore, M. Romanelli, P. Buxton, CRATOS-GS: A free-boundary, hierarchical adaptive mesh refinement Grad-Shafranov solver, *AIP Advances* 15 (9) (2025).
- [13] H. Heumann, J. Blum, C. Boulbe, B. Faugeras, G. Selig, J.-M. Ané, S. Brémond, V. Grandgirard, P. Hertout, E. Nardon, Quasi-static free-boundary equilibrium of toroidal plasma with CEDRES++: Computational methods and applications, *Journal of Plasma Physics* 81 (3) (2015) 905810301.
- [14] Z. Peng, Q. Tang, X.-Z. Tang, An adaptive discontinuous Petrov-Galerkin method for the Grad-Shafranov equation, *SIAM Journal on Scientific Computing* 42 (5) (2020) B1227–B1249.
- [15] D. A. Serino, Q. Tang, X.-Z. Tang, T. V. Kolev, K. Lipnikov, An adaptive newton-based free-boundary Grad-Shafranov solver, *arXiv preprint arXiv:2407.03499* (2024).
- [16] E. Howell, C. R. Sovinec, Solving the Grad-Shafranov equation with spectral elements, *Computer Physics Communications* 185 (5) (2014) 1415–1421.
- [17] J. Jepson, Importance of Grad-Shafranov re-solves towards accurately modeling an ITER equilibrium in NIMROD (2016).
- [18] D. Boffi, F. Brezzi, M. Fortin, et al., Mixed finite element methods and applications, Vol. 44, Springer, 2013.

- [19] D. N. Arnold, R. S. Falk, R. Winther, Finite element exterior calculus, homological techniques, and applications, *Acta numerica* 15 (2006) 1–155.
- [20] P. Bochev, A. Robinson, Matching algorithms with physics: exact sequences of finite element spaces, *Preservation of stability under discretization*, D. Estep and S. Tavener, eds., Philadelphia (2001) 145–165.
- [21] K. Hu, Y. Ma, J. Xu, Stable finite element methods preserving $\operatorname{div} \mathbf{B} = 0$ exactly for MHD models, *Numerische Mathematik* 135 (2) (2017) 371–396.
- [22] E. S. Gawlik, F. Gay-Balmaz, A finite element method for MHD that preserves energy, cross-helicity, magnetic helicity, incompressibility, and $\operatorname{div} \mathbf{B} = 0$, *Journal of Computational Physics* 450 (2022) 110847.
- [23] G. A. Wimmer, X.-Z. Tang, Structure preserving transport stabilized compatible finite element methods for magnetohydrodynamics, *Journal of Computational Physics* 501 (2024) 112777.
- [24] R. Anderson, J. Andrej, A. Barker, J. Bramwell, J.-S. Camier, J. Cervený, V. Dobrev, Y. Dudouit, A. Fisher, T. Kolev, W. Pazner, M. Stowell, V. Tomov, I. Akkerman, J. Dahm, D. Medina, S. Zampini, MFEM: A modular finite element methods library, *Computers & Mathematics with Applications* 81 (2021) 42–74.
- [25] S. Chandrasekhar, L. Woltjer, On force-free magnetic fields, *Proceedings of the National Academy of Sciences* 44 (4) (1958) 285–289.
- [26] A. T. McRae, G.-T. Bercea, L. Mitchell, D. A. Ham, C. J. Cotter, Automated generation and symbolic manipulation of tensor product finite elements, *SIAM Journal on Scientific Computing* 38 (5) (2016) S25–S47.
- [27] MFEM: Modular finite element methods [Software], mfem.org. doi:10.11578/dc.20171025.1248.
- [28] D. Green, X. Hu, J. Lore, L. Mu, M. L. Stowell, An efficient high-order numerical solver for diffusion equations with strong anisotropy, *Computer Physics Communications* 276 (2022) 108333.
- [29] C. J. Vogl, I. Joseph, M. Holec, Mesh refinement for anisotropic diffusion in magnetized plasmas, *Computers & Mathematics with Applications* 145 (2023) 159–174.